03,05

Electrochemical, magnetic and structural features of $Ni_{0.2}Zn_{0.8}Fe_2O_4$, nanoparticles synthesized under the conditions of thermal treatment of X-ray amorphous combustion products

© K.D. Martinson, D.D. Sakhno, P.V. Migunova, A.A. Lobinsky

Ioffe Institute,
St. Petersburg, Russia

E-mail: martinsonkirill@mail.ru

Received February 27, 2024
Revised February 27, 2024
Accepted February 28, 2024

For the first time, nickel-zinc ferrite nanopowder with the composition $Ni_{0.2}Zn_{0.8}Fe_2O_4$ was synthesized and physicochemically characterized by the method of thermal treatment of X-ray amorphous products of solution combustion method. It has been shown that ferrite formation occurs at a temperature of 465°C. A study of magnetic characteristics demonstrated that the resulting nickel-zinc ferrite nanopowder has a typical antiferromagnetic nature. The results obtained show the possibility of synthesizing X-ray amorphous combustion products of nanostructures with an average particle size of 24.8 nm, a degree of crystallinity of the order of 100%, and a specific surface area of 34.6 cm^2/g using thermal treatment.

Keywords: nickel-zinc ferrites, nanoparticles, solution combustion method, magnetic properties.

DOI: 10.61011/PSS.2024.04.58196.36

1. Introduction

Researchers from various countries have shown increased interest in obtaining nanostructured ferrite spinels of various compositions in recent years, which, among other things, is confirmed by the growing number of publications on this topic which has increased several times over the past ten years [1]. The growing relevance of ferrites can be explained primarily by their importance for a large number of practical applications. For instance, ferrites remain important and irreplaceable materials in the manufacture of sensors and sensors [2], various radio-electronic devices [3,4] and radio-absorbing coatings [5], despite the fact that spinel ferrites have been used in these industries for more than 60 years [6]. However, the development of new fields of application have started since the early 2000s, in which the main attention was paid to the dimensional characteristics of materials because which ferrite nanoparticles began to be actively used in the production of magnetically recoverable catalysts [7], MRI contrast agents [8], photocatalysts [9], antibacterial materials [10], in wastewater treatment [11] and etc. The expansion of possible applications of ferrites has led to a constant search for new methods for their production, since the classical solid-phase technology of the synthesis of ferrites, although solving the task of producing ceramic materials, is poorly suitable for the synthesis of nanostructures with a high degree of phase uniformity [11]. The search for new methods for obtaining ferrite nanopowders remains an important and urgent task from this point of view.

The specific field of application of functional materials based on spinel ferrites is primarily determined by their chemical and phase composition, morphological or microstructural features and structural parameters [12]. For this reason the method of synthesis is chosen with a special attention to the possibility of directed synthesis of nanostructures by controlling the synthesis parameters [13]. A large number of different methods for the synthesis of complex oxide nanoobjects including spinel ferrites are known to date with the most common being the solid-phase technology (where nanoparticles are obtained by processing in planetary or vibrating mills) [14], hydrothermal technology [15], sol-gel synthesis [16], co-precipitation method [17] and solution combustion method [18]. Each of these methods has its advantages and disadvantages; nevertheless, the solid-phase technology still remains optimal from the point of view of possible industrial scaling up, despite the complexity of obtaining small particles and synthesizing pure single-phase samples without impurity oxide phases [19,20]. However, new papers and patents have been published recently showing the possibility of producing significant volumes of ferrite powder using the solution combustion technique [21]. Moreover, the solution combustion method has significant advantages, such as the simplicity and speed of synthesis, the absence of specific requirements for complex and expensive equipment and a wide range of synthesis parameters, the control of which allows the synthesis of nanopowders with specified functional characteristics [22].

It should be noted that a set of advanced techniques have been developed in addition to the conventional direct method of solution combustion [23] for increasing the number of controlled synthesis parameters and improving the structural characteristics of the final products. They include the pulp and paper method of solution combustion [24], the method of combustion with microwave treatment [25],

combined sol-gel synthesis followed by combustion of the resulting gel [26] and a number of others. The authors of this paper developed an original synthesis technique based on the thermal treatment of X-ray amorphous combustion products. The original powder is produced with a significant excess or shortage of organic fuel because of which the synthesized sample has an amorphous structure with a low degree of crystallinity. Next, the amorphous powder is annealed in an air atmosphere.

This technique was successfully tested for the production of various complex oxide systems, including spinel ferrites and orthoferrites of rare earth elements [27–29]. This provides the first detailed study of the mechanism of formation of nickel-zinc ferrite of $Ni_{0.2}Zn_{0.8}Fe_2O_4$ composition using the technology described above with the characterization of basic physico-chemical properties of the produced nanopowder, determination of its characteristics and conclusions about the prospect of application of this technique for producing magnetic and electrochemical materials using the developed technology.

2. Experimental part

Crystallohydrates of the corresponding metals and glycine as an organic fuel and chelating agent were used as reagents for the synthesis of the initial X-ray amorphous nickel-zinc ferrite powder: $Zn(NO_3)_2 \cdot 6H_2O$ (chemically pure, Neva-Reaktiv), $Ni(NO_3)_2 \cdot 6H_2O$ (chemically pure, Neva-Reaktiv), $Fe(NO_3)_3 \cdot 9H_2O$ (chemically pure, Neva-Reaktiv), $C_2H_5NO_2$ (chemically pure, Neva-Reaktiv), HNO_3 (chemically pure, Neva-Reaktiv) and distilled water with an electrical resistivity of less than $5\,M\Omega \cdot cm$. The content of all the main components in the reagents used was in the range of 99.9%.

The synthesis technique is described in detail in previous papers of the authors [18,29]. At the first stage, a completely X-ray amorphous nickel-zinc ferrite powder of $Ni_{0.2}Zn_{0.8}Fe_2O_4$ composition was synthesized using iron, zinc and nickel nitrates with the addition of glycine in the quantity ensuring that the oxidation-reduction ratio φ equals to 0.1. All weighed quantities of crystallohydrates and glycine were collected according to the calculated values obtained in accordance with the reaction of formation of the target product, and dissolved in 40 ml of distilled water with constant stirring. Nitric acid was used to acidify the reaction solution for preventing precipitation containing complex compounds of transition metals. Then the resulting solution was heated on a ceramic tile to self-ignition point (almost complete boiling of water from the solution). A solid brown product was produced as a result, which was mechanically ground and annealed in a muffle furnace for 5 h at a temperature of 550°C to obtain nickel-zinc ferrite with a high proportion of the crystalline phase.

The choice of the heat treatment temperature was based on the results of differential thermal analysis (DTA) given in this paper. Shimadzu DTG-60 (DTA/TG mode) was used to perform DTA and thermogravimetric analysis (TGA). The powder was studied in an air atmosphere with a temperature range from 30 to 800°C, with a heating rate of 10°C/min.

The morphology and elemental composition of the synthesized ferrite were analyzed using scanning electron microscopy and energy dispersion spectroscopy with Tescan Vega 3 SBH scanning electron microscope equipped with Oxford INCA detector. The phase composition and structure of the resulting powder was analyzed using powder diffractometry with Rigaku smartLAB 3 diffractometer with $CuK_{\alpha 1}$-radiation (0.154056 nm) operated at 40 kV and 30 mA in the range from 20 to 80° 2θ, in increments 0.01° and accumulation time of 3 s. IJCD PDF-2 powder database was used to evaluate the phase composition. Infrared (IR) absorption spectra were acquired by IR Fourier spectroscopy using Shimadzu IRTracer-100 spectrometer in the wavenumber range from 3600 to 300 cm^{-1} using KBr tablets. Adsorption-structural analysis was performed for acquiring sorption–desorption isotherms using Micromeritics ASAP 2020 analyzer. The specific surface area values were calculated using the Brunauer–Emmett–Teller model (BET) embedded in the analyzer software. The magnetic parameters of the synthesized powder were studied using Lake Shore 7410 vibration magnetometer at room temperature (278 K) in the field range up to 60,000 Oe with a standard cuvette. The curves of cyclic voltammetry (CVA) were recorded in an alkaline electrolyte 1M KOH in the range from −1700 to 700 mV relative to the silver chloride electrode. A suspension with nafion in isopropanol was prepared for application to the working electrode (which was composed of synthesized powder).

3. Results and discussion

3.1. DTA and TGA

Figure 1 shows the DTA/TGA curves of the initial sample of nickel-zinc ferrite without heat treatment with a low fraction of the crystalline phase.

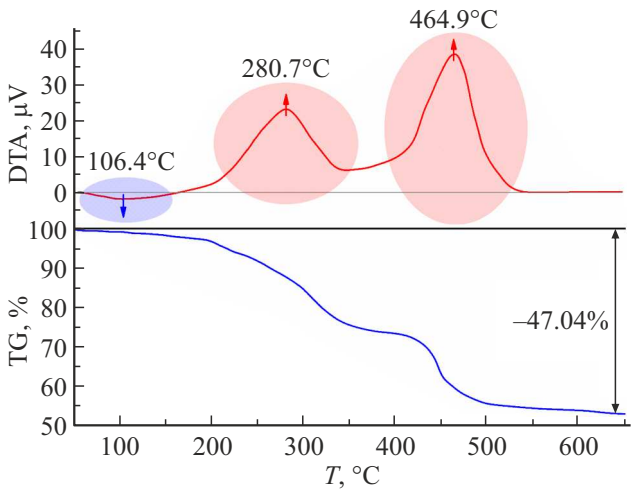

Figure 1. DTA/TGA curves of the initial X-ray amorphous nickel-zinc ferrite powder.

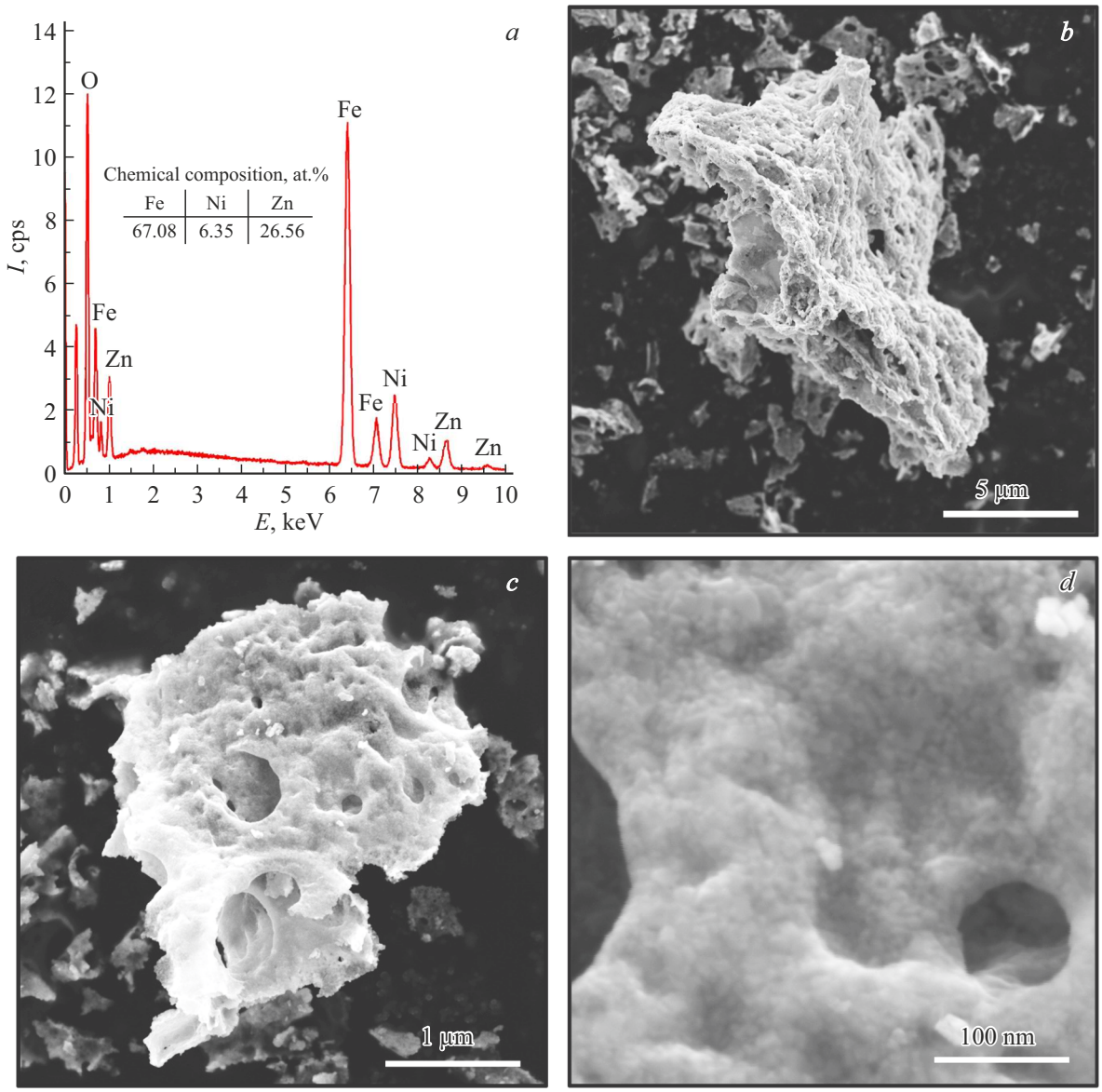

Figure 2. Energy dispersion spectrum (*a*) and micrographs of nickel-zinc ferrite annealed at 550°C at magnification 5 μm (*b*), 1 μm (*c*) and 100 nm (*d*).

This analysis was primarily needed for determining the temperature of ferrite formation and, as a result, for selection of the appropriate annealing temperature. The first endothermic effect is observed at 106.4°C and it corresponds to the removal of the adsorbed and crystalline water. It is possible to assume that despite the absence of heat treatment, a small amount of crystalline water was present in the initial sample given the low intensity of this effect. The following observed effect at 280.7°C is exothermic and characterizes the process of oxidation of glycine residues that did not participate in the ferrite formation reaction. This process is accompanied by abundant release of gaseous products (CO, CO_2, NO, NO_2, etc.) and is described in detail in many papers devoted to the obtaining of oxide systems by the solution combustion method [19,30]. It should be noted that this the process during which an increase of the rate of mass loss of the sample is observed, which also confirms the glycine oxidation.

Finally, the last and most intense exothermic effect at 464.9°C corresponds to the process of decomposition of the initial amorphous mass and crystallization of ferrite. A small halo on the mass loss curve indicates that initially (approximately at 440–450°C) the decomposition of metal nitrates takes place, which followed by the crystallization of ferrite from the amorphous phase and a mixture of precursors. The actual loss of mass stops with the end of these processes. In case of the absence of any other effects on the DTA curve, it is possible to speak about the end of the formation of nickel-zinc ferrite and the absence of other phase changes in the studied initial composition. The total mass loss during all the processes described above is 47.04%. The obtained data made it possible to determine

the optimal temperature of heat treatment of the initial X-ray amorphous powder for completing the nickel-zinc ferrite formation and crystallization process — 550°C.

3.2. Chemical composition and morphology

An elemental analysis was performed using energy dispersion spectroscopy for determining the conformance of the obtained ferrite with the calculated composition (Figure 2, *a*). The produced composition corresponds to nickel-zinc ferrite $Ni_{0.2}Zn_{0.8}Fe_2O_4$ within the error of the determination method according to the results shown in the figure. The table shown in the figure for convenience contains a recalculation without taking into account oxygen (an area of about 0.5keV) which is determined using X-ray methods with a fairly high error, and carbon (an area of about 0.4keV) the presence of which is associated with the use of carbon adhesive tape in the analysis of the sample. The powder was studied in five different points with an area of $1.5 \times 1.5\,mm^2$ to check the homogeneity of the chemical composition of the sample. The results of the study confirmed that the obtained results of the analysis of the main elements in all the studied areas differ by no more than 0.5%.

The morphology of synthesized nickel-zinc ferrite is shown in Figure 2, *b*–*d*. The micrographs shown in Figure 2, *b* and *c* demonstrate typical porous micron agglomerates characteristic of solution combustion products consisting of nanoparticles (which follows from Figure 2, *d*). Figure 2, *d* allows indirectly estimating the average size of the obtained nanoparticles and confirms that their size is less than 100 nm. It was found using ImageJ software package that the average particle size in the studied area is approximately 15–20 nm.

3.3. Phase composition and structural parameters

The X-ray diffraction analysis was performed for confirmation of the phase composition of the obtained nickel-zinc ferrite and the results of this analysis are shown in Figure 3.

The results of the X-ray diffraction analysis demonstrate that the synthesized powder is a single-phase nickel-zinc ferrite with a spinel structure (space group $Fd3m$, JCPDS card #080234). The lattice cell parameters were refined using the Rietveld method that provided the following values: $a = b = c = 8.425(3)$ Å, which is close enough to the reference value. Refinement quality is $R_w = 1.32\%$. The fraction of the crystalline phase was estimated using an internal standard (cubic silicon α-Si) and amounted to 99%. The average size of crystallites was calculated using the Scherrer formula and turned out to be 22 nm, which is in good agreement with the results obtained using the method of fundamental parameters for constructing the size distribution of crystallites (average size 24.8 nm) and with data obtained from micrographs (Figure 2, *d*, of the order of 20 nm). The crystallite size distribution constitutes a unimodal distribution and is almost symmetrical.

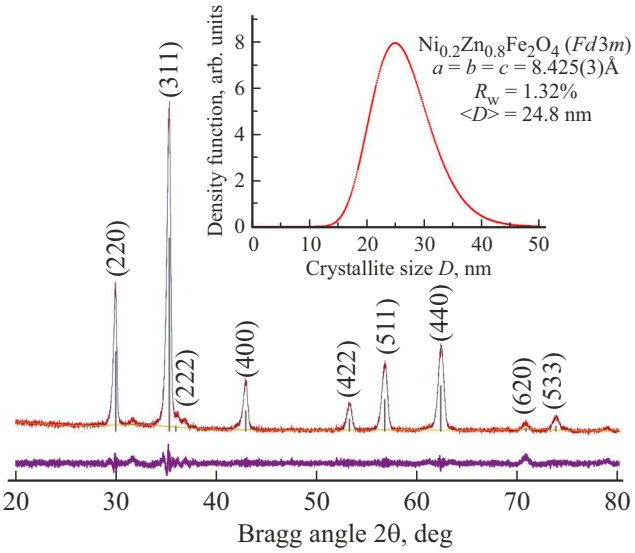

Figure 3. Diffraction pattern and crystallite size distribution of the synthesized and annealed sample of $Ni_{0.2}Zn_{0.8}Fe_2O_4$.

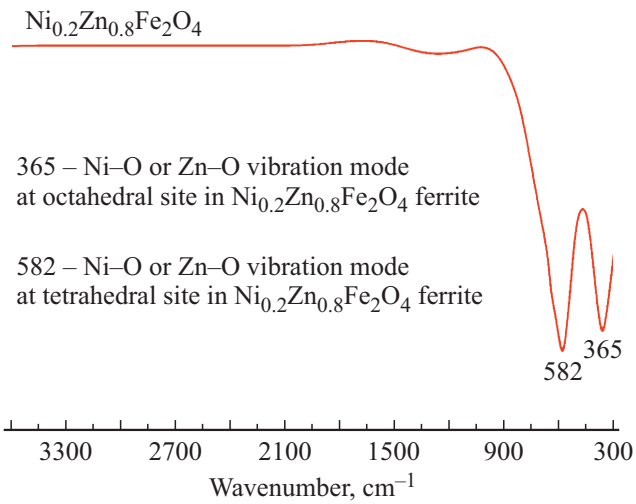

Figure 4. IR spectra of the annealed nickel-zinc ferrite sample.

In addition, the IR spectrum of the annealed sample was obtained to confirm the structure, which is shown in Figure 4. The absence of absorption bands in the region of 3600 and 1600 cm^{-1} confirms the removal of adsorbed and crystalline water from the sample (this process occurs at 100°C according to DTA data). In addition, the samples lack characteristic absorption bands for valence and deformation vibrations of N–O bonds in nitrates, which also indicates the completed process of ferrite formation. Two single absorption bands in the region 582 and 365 cm^{-1} are associated with valence vibrations of Ni–O or Zn–O bonds in octahedral and tetrahedral positions of nickel-zinc ferrite and were repeatedly described in previous papers studying similar systems [31]. Thus, the results of IR Fourier spectroscopy confirm the data of X-ray diffraction analysis and indicate the successful synthesis of nickel-zinc ferrite.

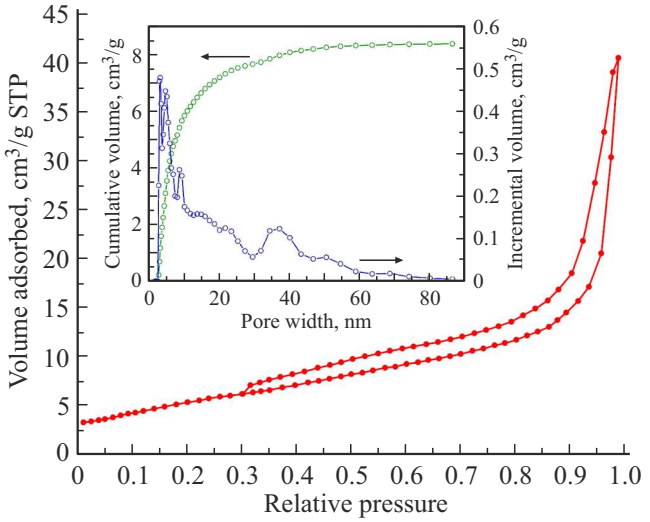

Figure 5. The nitrogen adsorption–desorption isotherm and the results of constructing the pore size distribution calculated on the basis of BJH desorption pore volume data.

3.4. Adsorption-structural analysis

The textural features of the synthesized powder were studied by low-temperature adsorption–desorption of nitrogen. Figure 5 shows the resulting isotherm, which can be classified as type IV according to the UPAC classification. It is possible to make a conclusion about the mesoporous nature of the synthesized material taking into account the type of isotherm and the results of pore size construction. The nature of the distribution clearly demonstrate that most of the pores are concentrated in the region from 5 to 10 nm. The specific surface area values were calculated using the linear form of the BET equation and amounted to 34.6 cm^2/g.

The analysis of the obtained isotherm together with the results of scanning electron microscopy suggests that the nanopowder is a foamy substance containing ferrite nanoparticles in the interstitial spaces, which, in turn, should ensure their availability for both catalytic and electrochemical processes.

3.5. Magnetic properties

The magnetic hysteresis ($M-H$-) loops were obtained using a vibration magnetometer and are shown in Figure 6.

The values of saturation magnetization M_s, residual magnetization M_r and coercive force H_c are 20.72 emu/g, 2.87 emu/g and 94.3 Oe, respectively, according to the obtained results. The magnetic values slightly change upwards compared with pure zinc ferrite because of the substitution of zinc cations by nickel cations in octahedral and tetrahedral positions of the crystal lattice. The size of the ferrite particles also influences magnetic properties. However, no significant decrease of the coercive force is observed taking into account the fact that the particle size is significantly higher than the size of a single domain (in the order of 11 nm, for this type of system). Thus, the synthesized powder is a classic antiferromagnetic material, which is typical for mixed nickel-zinc ferrites. Nevertheless, the decrease of the synthesis temperature and reduction of the heat treatment time allow obtaining single-domain particles in theory and thereby significantly changing the nature of the magnetic behavior of the synthesized material, which is an additional advantage of the proposed technology.

3.6. Electrochemical properties

The electrochemical characteristics of the nanopowder of $Ni_{0.2}Zn_{0.8}Fe_2O_4$ ferrite were studied by the CVA method (Figure 7).

Measurements were performed in an alkaline electrolyte 1M KOH in the range from 1700 up to 700 mV relative

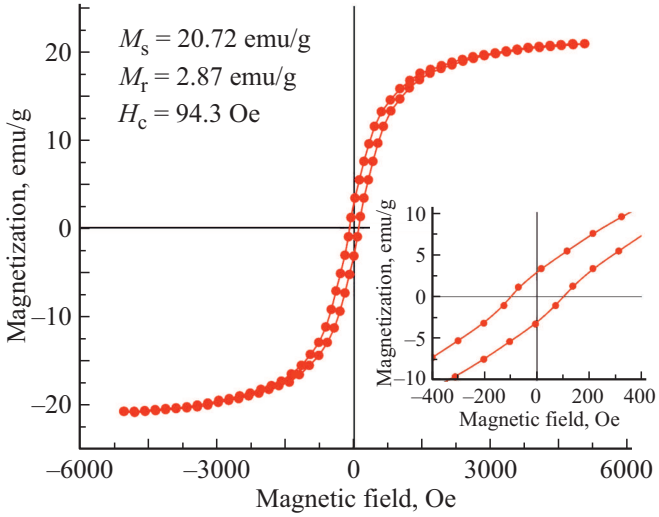

Figure 6. Magnetic hysteresis ($M-H$-) loops of annealed nickel-zinc ferrite of $Ni_{0.2}Zn_{0.8}Fe_2O_4$ composition obtained at room temperature.

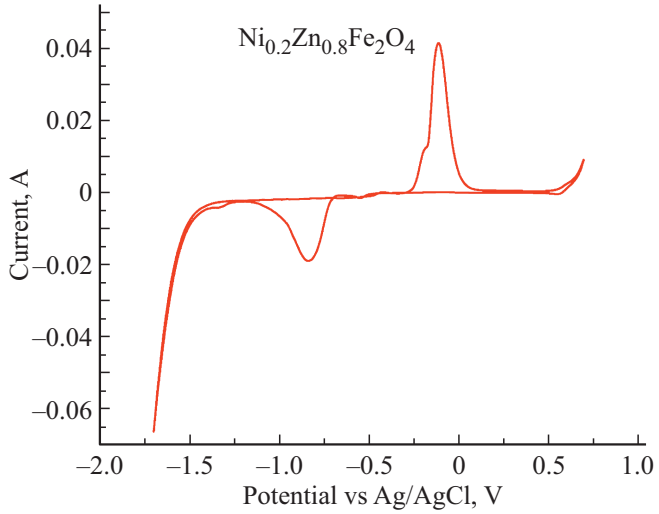

Figure 7. Cyclic voltammetry curve of synthesized nickel-zinc ferrite thermally treated at 550°C for 5 h.

to the silver chloride electrode. The scanning rate was 10 mV/s in the potential window of −2−1.0 V. The wide anode peak is located at −0.7 V, whereas the cathode peak is at −0.08 V. Apparently, the charge is retained due to reversible oxidation-reduction processes Fe^{3+}/Fe^{2+} in the electrode. Thus, the resulting powder is a promising material for producing highly efficient cathode materials for Zn-ion supercapacitors.

4. Conclusion

According to the results of the conducted studies a nanopowder of nickel-zinc ferrite with $Ni_{0.2}Zn_{0.8}Fe_2O_4$ composition was synthesized for the first time under the conditions of heat treatment of X-ray amorphous products of solution combustion. The synthesis included a two-stage process using the direct solution combustion method with a significant shortage of organic fuel for obtaining the initial amorphous powder and its subsequent heat treatment at a temperature of 550°C for 5 h. It was found that ferrite is formed at at 480°C under the selected conditions. The selected temperature regime ensures the production of nanocompositions with an average size of about 20−24 nm and a degree of crystallinity of the order of 99%. The studies of magnetic and electrochemical properties demonstrated that the synthesized ferrite has a typical antiferromagnetic nature of behavior and is a promising material for producing Zn-ion supercapacitors.

Acknowledgments

The authors of the paper would like to express their gratitude to the Engineering Center of the St. Petersburg State Institute of Technology (Technological University) for their assistance in conducting a study of morphology and its structure.

Funding

This study was supported by grant No. 21-73-10070 from the Russian Science Foundation.

Conflict of interest

The authors declare that they have no conflict of interest.

References

[1] O.D. Dastjerdi, H. Shokrollahi, S. Mirshekari. Inorg. Chem. Commun. **153**, 110797 (2023).
[2] R. Ranga, A. Kumar, P. Kumari, P. Singh, V. Madaan, K. Kumar. Mater. Characterizations **178**, 111269 (2021).
[3] S.J. Salih, W.M. Mahmood. Heliyon **9**, *6*, e16601 (2023).
[4] K.D. Martinson, I.B. Panteleev, K.A. Steshenko, V.I. Popkov. J. Eur. Ceram. Soc. **42**, *8*, 3463 (2022).
[5] D.S. Aherrao, C. Singh, A.K. Srivastava. J. Appl. Phys. **132**, *24*, 240701 (2022).
[6] M. Sugimoto. J. Am. Ceram. Soc. **82**, *2*, 269 (1999).
[7] M. Amiri, K. Eskandari, M. Salavati-Niasari. Adv. Colloid. Interface Sci. **271**, 101982 (2019).
[8] M.D. Shultz, S. Calvin, P.P. Fatouros, S.A. Morrison, E.E. Carpenter. J. Magn. Magn. Mater. **311**, *1*, 464 (2007).
[9] N.K. Gupta, Y. Ghaffari, S. Kim, J. Bae, K.S. Kim, M. Saifuddin. Sci. Rep. **10**, *1*, 4942 (2020).
[10] M.I.A.A. Maksoud, G.S. El-Sayyad, H.S. El-Bastawisy, R.M. Fathy. RSC Adv. **11**, *45*, 28361 (2021).
[11] S.B. Narang, K. Pubby. J. Magn. Magn. Mater. **519**, *6*, 167163 (2021).
[12] R. Sagayaraj, S. Aravazhi, G. Chandrasekaran. Int. Nano Lett. **11**, *4*, 307 (2021).
[13] A. Kumar, S. Dutta, S. Kim, T. Kwon, S.S. Patil, N. Kumari, S. Jeevanandham, I.S. Lee. Chem. Rev. **122**, *15*, 12748 (2022).
[14] Y. Cao, H. Qin, X. Niu, D. Jia. Ceram. Int. **42**, *9*, 10697 (2016).
[15] N.M. Refat, M.Y. Nassar, S.A. Sadeek. RSC Adv. **12**, *38*, 25081 (2022).
[16] M. Sajjia, M. Oubaha, M. Hasanuzzaman, A.G. Olabi. Ceram. Int. **40**, *1*, 1147 (2014).
[17] K. Maaz, S. Karim, A. Mumtaz, S.K. Hasanain, J. Liu, J.L. Duan. J. Magn. Magn. Mater. **321**, *12*, 1838 (2009).
[18] K.D. Martinson, A.D. Beliaeva, D.D. Sakhno, I.D. Beliaeva, V.E. Belyak, G.G. Nianikova, I.B. Panteleev, V.N. Naraev, V.I. Popkov. Water **14**, *3*, 454 (2022).
[19] A. Varma, A.S. Mukasyan, A.S. Rogachev, K.V. Manukyan. Chem. Rev. **116**, *23*, 14493 (2016).
[20] S. Gaffar, A. Kumar, U. Riaz. J. Electroceram. **51**, *4*, 246 (2023).
[21] A.S. Mukasyan, P. Epstein, P. Dinka. Proceed. Combustion Institute **31**, *2*, 1789 (2007).
[22] F. Siddique, S. Gonzalez-Cortes, A. Mirzaei, T. Xiao, M.A. Rafiq, X. Zhang. Nanoscale **14**, *33*, 11806 (2022).
[23] E. Novitskaya, J.P. Kelly, S. Bhaduri, O.A. Graeve. Int. Mater. Rev. **66**, *3*, 188 (2020).
[24] A. Kumar. Industrial & Engineering Chem. Res. **58**, *19*, 7681 (2019).
[25] M. Venkatesh, G.S. Kumar, S. Viji, S. Karthi, E.K. Girija. Modern Electron. Mater. **2**, *3*, 74 (2016).
[26] B. Niu, F. Zhang, H. Ping, N. Li, J. Zhou, L. Lei, J. Xie, J. Zhang, W. Wang, Z. Fu. Sci. Rep. **7**, *1*, 3421 (2017).
[27] K.D. Martinson, I.A. Cherepkova, V.V. Sokolov. Glass Phys. Chem. **44**, *1*, 21 (2018).
[28] S.V. Dyachenko, K.D. Martinson, I.A. Cherepkova, A.I. Zhernovoi. Russ. J. Appl. Chem. **89**, *4*, 535 (2016).
[29] K.D. Martinson, I.S. Kondrashkova, M.I. hebanenko, A.S. Kiselev, T.Yu. Kiseleva, V.I. Popkov. J. Rare Earths **40**, *2*, 296 (2022).
[30] R.M. Borade, S.B. Somvanshi, S.B. Kale, R.P. Pawar, K.M. Jadhav. Mater. Res. Express **7**, *1*, 016116 (2020).
[31] R. Rameshbabu, R. Ramesh, S. Kanagesan, A. Karthigeyan, S. Ponnusamy. J. Supercond. Novel Magn. **27**, *6*, 1499 (2014).

Translated by A.Akhtyamov